Real-time microstructure of shocked LiF crystals: Use of synchrotron x-rays

Stefan J. Turneaure,[1,a)] Y. M. Gupta,[1] K. Zimmerman,[1] K. Perkins,[1] C. S. Yoo,[2] and G. Shen[3]
[1]*Institute for Shock Physics and Department of Physics, Washington State University, Pullman, Washington 99164, USA*
[2]*Institute for Shock Physics and Department of Chemistry, Washington State University, Pullman, Washington 99164, USA*
[3]*HPCAT and HPSynC, Geophysical Laboratory, Carnegie Institution of Washington, Argonne, Illinois 60437, USA*

(Received 3 November 2008; accepted 9 January 2009; published online 12 March 2009)

We describe the use of a third generation synchrotron facility to obtain *in situ*, real-time, x-ray diffraction measurements in plate impact experiments. Subnanosecond duration x-ray pulses were utilized to record diffraction data from pure and magnesium-doped LiF single crystals shocked along the [111] and [100] orientations. The peak stresses were 3.0 GPa for the [111] oriented LiF and between 3.0 and 5.0 GPa for the [100] oriented LiF. For these stresses, shock compression along [111] results in elastic deformation and shock compression along [100] results in elastic-plastic deformation. Because of the quality of the synchrotron x-ray pulses, both shifting and broadening of the diffraction data were obtained simultaneously. As expected, shifts for elastic compression and elastic-plastic compression in shocked LiF were consistent with uniaxial and isotropic lattice compression, respectively. More importantly, diffraction patterns from crystals shocked along [100] exhibited substantial broadening due to elastic-plastic deformation. The broadening indicates that the shocked LiF(100) crystals developed substructure with a characteristic size for coherently diffracting domains (0.1–10 μm) and a distribution of (100) microlattice-plane rotations ($\sim 1°$ wide). In contrast to the LiF(100) results, broadening of the diffraction pattern did not occur for elastically deformed LiF(111). Another important finding was that the amount of lattice disorder for shocked LiF(100) depends on the loading history; the broadening was larger for the magnesium-doped LiF(100) (large elastic precursor) than for ultrapure LiF(100) (small elastic precursor) shocked to the same peak stress. The data are simulated by calculating the diffraction pattern from LiF(100) with a model microstructure consisting of coherently diffracting domains. The lattice orientation and longitudinal strain is assumed uniform within domains, but they vary from domain to domain with Gaussian distributions. Simulations using such a model are in good agreement with the measured diffraction patterns. The principal finding from the present work is that synchrotron x-rays can provide real-time data regarding microstructure changes accompanying shock-induced deformation and structural changes. © *2009 American Institute of Physics*. [DOI: 10.1063/1.3080176]

I. INTRODUCTION

Shock wave compression of materials results in large and near-discontinuous changes in stress, density, and internal energy.[1] As such, shock wave experiments in combination with real-time measurements of crystal structure changes and lattice deformation, at picosecond-nanosecond time scales, are uniquely suited to understand condensed matter phenomena at extreme conditions. Planar shock waves, generated by flyer plate impacts or laser drives or high explosives, result in a state of macroscopic uniaxial strain in the material. To date, shock wave experiments have been dominated by continuum measurements. Since the work of Johnson *et al.*,[2] the use of x-rays to probe the microscopic response of shocked solids has been a subject of interest. For single crystals shocked elastically along a principal axis, the uniaxial compression condition persists down to the lattice level.[3] Above a threshold shock wave amplitude (the elastic limit), the crystal is unable to sustain the large stress deviators associated with elastic compression, and elastic-plastic deformation occurs on nanosecond or shorter time scales.

Although the macroscopic strain state during elastic-plastic deformation remains uniaxial due to plane wave loading, irreversible atomic motion occurs to limit or reduce the stress deviators in the crystal and the resulting lattice deformation is not uniaxial. This finding has been demonstrated experimentally using real-time x-ray diffraction (XRD) measurements; the lattice compression (on average) behind the plastic shock wave was found to be nearly isotropic (corresponding to minimal stress deviators) for elastic-plastic deformation in shocked LiF,[3–6] NaCl,[7] and Cu (Ref. 8) crystals. However, these experiments did not provide information regarding microstructural changes that occur during shock-

a)Electronic mail: stefant@wsu.edu.

induced plastic deformation. Because of a lack of real-time microstructural data, the micromechanisms that govern lattice changes during the transition from elastic deformation to elastic-plastic deformation under shock compression are not well established. Synchrotron x-rays have the requisite spectral and spatial characteristics to probe material microstructure during shock compression.

Theoretical attempts to understand shock-induced plasticity at the microscopic level consist of postulated descriptions ranging from simple dislocation based pictorial models[9–13] to more complex molecular dynamics (MD) simulations.[14,15] The latter can, in principle, provide detailed microscopic information regarding elastic-plastic deformation during the stress relaxation process in shocked crystals. However, realistic MD simulations of crystalline solids with appropriate lattice defects and experimental validation of such simulations remain a significant and an outstanding challenge. Experimental efforts to understand micromechanisms governing shock-induced elastic-plastic deformation have also included an examination of the crystal microstructure in recovered samples.[9,13,16,17] However, the complex loading and unloading histories and the large deviations from uniaxial strain prior to sample recovery[18] make it nearly impossible to correlate the observed postshock microstructure to initial shock wave loading conditions (approximately nanoseconds). Thus, real-time measurements of shock-induced microstructure, while the sample remains under macroscopic uniaxial strain, constitute a long standing scientific need. Such measurements are, however, extremely challenging because data have to be obtained in nanoseconds in single event experiments.

Here, we report on the use of XRD measurements on shocked crystals to provide real-time data on microstructural changes and lattice compression simultaneously in plate impact experiments. This advance was made possible by combining a compact impact facility with a third generation synchrotron x-ray source to achieve the resolution required to determine the microstructural response.[19] The compact impact facility was designed and developed specifically for the experiments reported here.

LiF was chosen as the prototype material for shock wave experiments performed at the Advanced Photon Source at the Argonne National Laboratory. The shock wave response of pure and Mg-doped LiF has been studied extensively at the continuum level since the 1970s (Refs. 20–24) and anisotropic continuum models using a dislocation dynamics framework have been used to simulate the data.[25] Typical stress wave profiles for pure LiF shocked along [111] and [100], and Mg-doped LiF shocked along [100] are shown schematically in Fig. 1. The shock response of LiF exhibits large anisotropy: for [100] loading, an elastic-plastic response occurs[20,21] as seen by the two-wave structure in Fig. 1; whereas for [111] loading up to 4 GPa, a purely elastic response occurs.[22,23] Also, the elastic-plastic response along [100] is strongly dependent on Mg doping.[20,21] Despite the large differences in the loading paths for pure and Mg-doped samples,[20,21] as shown in Fig. 1, the average lattice compressions in the peak state were nearly identical and isotropic.[3–6] Clearly, the average lattice compression cannot distinguish between loading history effects.

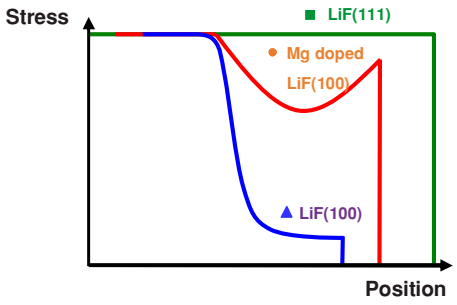

FIG. 1. (Color online) Schematic illustration of shock wave profiles propagating from left to right in LiF single crystals. For LiF shocked along [111], a single elastic wave propagates. For LiF shocked along [100], a two-wave structure propagates consisting of an elastic wave and a slower traveling plastic wave. The Mg-doped LiF and the pure LiF shocked along [100] exhibit large and small amplitude elastic waves, respectively.

The objectives of this first study were as follows: to establish the feasibility of using a synchrotron for real-time XRD measurements in plate impact experiments, to determine microstructural changes due to shock-induced elastic-plastic deformation in LiF, and to examine how variations in loading history, as shown in Fig. 1 for pure and Mg-doped LiF(100), influence microstructural changes. Experiments on LiF shocked along [111], corresponding to elastic deformation, provided a reference.

The article is organized as follows. Section II provides an overview of the experimental method. The experimental results are summarized in Sec. III. The analysis of our results and the corresponding discussion are presented in Sec. IV. Main findings from this work are presented in Sec. V.

II. EXPERIMENTAL METHOD

Figures 2 and 3 show a schematic view and a picture of the experimental setup located in hutch 16ID-D at the Advanced Photon Source, respectively. A flat-faced Al6061 projectile was accelerated down a $\frac{1}{2}$ in. diameter barrel to a velocity U_{pr} using commercially available gun powder and

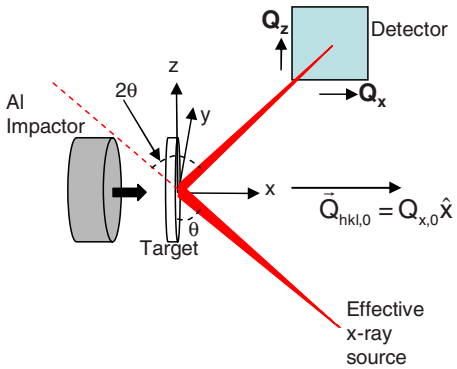

FIG. 2. (Color online) Sketch of the experimental arrangement. The ambient LiF crystal is oriented with a particular reciprocal lattice vector, $\vec{Q}_{hkl,0}$, nominally parallel to the impact direction (x-axis). 2θ is the scattering angle. The distance from the effective x-ray source to the sample (400 mm) is equal to the distance from the sample to the area detector. The face of the detector is perpendicular to the diffracted beam.

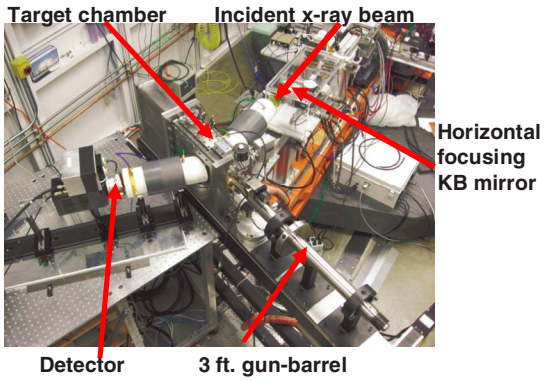

FIG. 3. (Color online) Picture of the experimental setup in hutch 16ID-D of HPCAT at the Advanced Photon Source.

cartridges. The projectile impacted a 10 mm diameter disk shaped target consisting of the LiF sample sandwiched between a z-cut quartz buffer (Meller Optics, Providence, RI) and a vitreous carbon (VC) x-ray window (Atomergic Chemetals, Melville, NY). Upon impact, a shock wave propagated through the quartz and the LiF sample to the LiF/VC interface, where a partial reflection of the shock wave occurs due to the mechanical impedance mismatch between the LiF and VC. The single pulse XRD measurement (8.8 keV x-rays with ~100 ps duration) was made after the reflected wave at the LiF/VC interface had traveled more than ~70 μm (x-ray penetration depth) back into the LiF but before any other wave reflections from the VC free surface or quartz arrived at the probed region of the LiF. Thus, the probed region of the sample was in a constant stress state.

Three types of LiF samples were used in the experiments. Ultrapure LiF(100) samples were obtained as disks from Saint-Gobain Crystals (Solon, OH). The pure LiF(111) sample was cut from a boule obtained from the University of Utah. The 120 ppm Mg-doped LiF(100) samples were cleaved from a boule also obtained from the University of Utah. The Mg-doped LiF samples were heat treated, air quench, followed by an anneal II treatment, as described in Ref. 21. The crystal orientations of the LiF samples were within 3° of their nominal orientations. Table I lists the projectile velocity (U_{pr}), LiF properties, and the target piece thicknesses for each experiment.

The XRD measurements were performed using the standard 24 bunch mode (x-ray pulses arrive periodically at the sample with 153.4 ns spacing between x-ray pulses) at the Advanced Photon Source. Because the impact event and the synchrotron x-ray pulses were not temporally correlated, the experiments were designed such that the probed region of the LiF was in a constant stress state (and under macroscopic uniaxial strain) for a duration longer than the 153.4 ns x-ray spacing between x-ray pulses. This feature ensured that an x-ray pulse would arrive at the probed region of the sample while the sample was in the desired uniform shocked state. The diffracted x-rays from the desired incident pulse were isolated from the diffracted x-rays from the many other incident pulses by using a gated intensified x-ray detector consisting of P47 phosphor, a Photek microchannel plate image intensifier, and a Princeton Instruments charge-coupled device with 20 μm pixel size. The detector was gated on just prior to the desired x-ray pulse arriving at the detector and gated off just prior to the next x-ray pulse arriving at the detector.

The XRD geometry shown in Fig. 2 is similar to that in Refs. 3 and 6. However, in the present work, x-rays are significantly more monochromatic ($\Delta E/E \approx 10^{-4}$) and the x-ray beam divergence is much better controlled. Kirkpatrick–Baez (KB) mirrors and x-ray slits were used to create the effective x-ray source shown in Fig. 2. A 1 m long Rh coated KB mirror, located about 10 m upstream of the sample, was used to focus the beam vertically with the focus somewhat upstream of the sample. A 200 mm long Rh coated KB mirror located about 600 mm upstream from the sample was used to focus the beam horizontally to an approximately 30 μm width located 400 mm in front of the sample. The beam incident on the LiF contained 2×10^5 photons/pulse, was nearly collimated vertically, and diverged horizontally from the effective source with a full angular width of about 0.2°. The effective x-ray source size and the vertical divergence of the x-rays are significantly smaller than for experiments performed using the flash x-ray system described in Refs. 3 and 6. These experimental improvements provided us with the measurement resolution needed to examine the LiF microstructure. The measured microstructure is an average over the crystal volume that was exposed to the horizontally diverging beam (~4 mm wide, ~200 μm tall, and ~70 μm deep).

For the (111) and (100) oriented LiF samples, the 111 (17.65° ambient Bragg angle) and 200 (20.50° ambient Bragg angle) peaks were monitored, respectively. The following procedure was followed prior to each shock wave

TABLE I. Experimental parameters.

Expt.	U_{pr} (mm/μs)	LiF orientation	Orientation deviation (deg)	Mg doping (ppm)	Transverse LiF orientation[a] (degrees)	Sample thickness (μm)	Quartz thickness (μm)	VC thickness (μm)
1 (07–936)	0.344	(111)	2.7	···	22	807	2017	506
2 (07–947)	0.402	(100)	2.8	···	35	602	2018	547
3 (07–937)	0.491	(100)	2.0	···	18	599	2017	542
4 (07–942)	0.658	(100)	0.7	···	3	594	2018	543
5 (07–946)	0.401	(100)	1.8	120	39	605	2017	553
6 (07–938)	0.503	(100)	0.1	120	22	601	2017	554
7 (07–943)	0.667	(100)	0.3	120	44	599	2017	547

[a]We define the transverse LiF orientation in terms of a rotation of the LiF sample about the shock loading direction (x-axis). For LiF(111) 0° corresponds to $[1\bar{1}0]$ vertical (along the z-axis). For LiF(100) 0° corresponds to [001] vertical (along the z-axis).

TABLE II. Experimental results.

Expt.	Input LiF stress (GPa)	Reflected LiF/VC interface stress(GPa)	X-ray measurement time after impact (ns)	$\Delta\Phi_y$, in shocked state FWHM(deg)	ΔQ_x in ambient state FWHM(μm^{-1})	ΔQ_x in shocked state FWHM(μm^{-1})
1 (07–936)	3.04	1.65	453	0.03(0.05)	4.3(0.8)	4.2(0.8)
2 (07–947)	2.97	2.03	470	0.37(0.08)	3.3(0.8)	8.5(1.2)
3 (07–937)	3.65	2.47	511	0.51(0.17)	3.0(0.8)	9.4(1.6)
4 (07–942)	4.96	3.26	454	0.92(0.29)	3.7(0.8)	12.4(2.3)
5 (07–946)	2.97	2.04	476	0.68(0.16)	3.1(0.8)	9.0(1.8)
6 (07–938)	3.74	2.54	526	0.80(0.26)	3.1(0.8)	12.8(2.0)
7 (07–943)	5.04	3.31	504	1.22(0.33)	2.9(0.8)	14.8(2.7)

experiment. The target was positioned in the target chamber of the impact launcher so that the back of the LiF sample was centered on the incident diverging beam to better than 0.5 mm. The proper beam/sample angle for the particular *hkl* peak under investigation was determined by using a calibrated *p-i-n* diode to record the diffracted intensity as a function of the incident beam/sample angle. Gaussian fits to the diffracted intensity versus beam/sample angle had full widths at half maximum (FWHM) of about 0.2° (equal to the incident beam divergence). This confirms that the ambient crystals were of reasonably high quality. Prior to the shock wave experiment, an ambient diffraction pattern was obtained with a single x-ray pulse.

III. RESULTS

Table II lists the LiF input stresses, LiF/VC interface stresses, and times relative to impact at which the diffraction measurements occurred. Representative diffraction patterns measured with a single x-ray bunch from the synchrotron are shown in Figs. 4(a)–4(d). The images correspond to an 8 $\times$ 8 mm^2 area on the detector. The images have been mapped linearly into reciprocal space. For the geometry used, the horizontal axis maps into Q_x and the vertical detector axis maps into Q_z.

The sizes of the preshock diffraction patterns for LiF(111) [Fig. 4(a)] and Mg-doped LiF(100) [Fig. 4(c)] were primarily due to instrumental broadening. The vertical instrumental broadening is due to the ~200 μm beam height and the horizontal instrumental broadening is due to the x-ray bandwidth ($\Delta E/E$), the finite x-ray source width, the x-ray penetration into the LiF sample, and the spatial resolution of the detector.

The corresponding diffraction patterns obtained while the LiF samples were shock compressed (to comparable stresses) are shown in Figs. 4(b) and 4(d) for LiF(111) (elastic compression) and Mg-doped LiF(100) (elastic-plastic compression), respectively. The differences are quite dra-

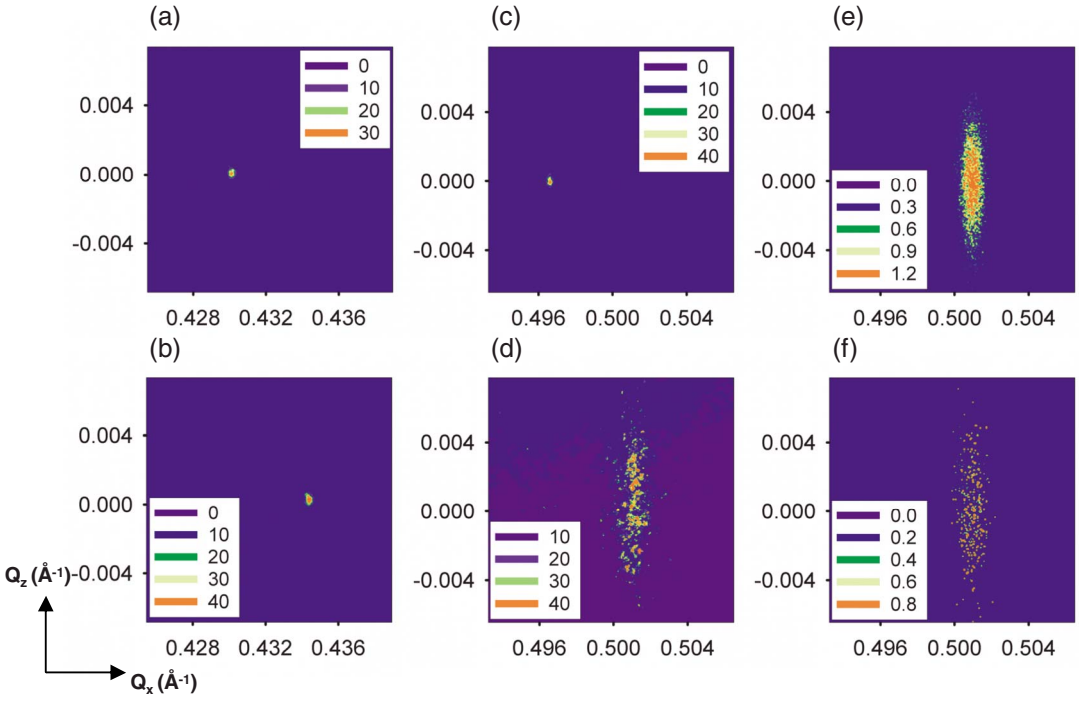

FIG. 4. (Color online) Representative 8 $\times$ 8 mm^2 diffraction images for which the real space coordinates have been mapped linearly into reciprocal space. (a) and (b) show images from Expt. 1 of the 111 peak from unshocked and shocked LiF(111), respectively. (c) and (d) show images from Expt. 5 of the 200 peak from unshocked and shocked Mg-doped LiF(100), respectively. (e) and (f) show diffraction patterns, using two different sets of microstructural parameters, to simulate the experimental data shown in (d). All intensity scales have arbitrary units.

matic. For elastic loading along [111], the diffraction pattern shifted to higher Q_x which indicates lattice compression; but the size of the diffraction pattern did not change, indicating no substructure as expected for elastic compression. For elastic-plastic loading along [100], the diffraction pattern shifted to higher Q_x which indicates lattice compression, but the diffraction pattern was significantly spread over a range of Q_x and Q_z values. The spreading demonstrates that the single crystal developed substructure as a result of elastic-plastic deformation due to shock compression. This point is discussed in detail in Sec. IV. The graininess of the image observed in Fig. 4(d) is partly a result of the number of diffracted photons ($\sim 10^3$) reaching the detector during the single bunch measurement. Five other experiments on both pure and Mg-doped LiF(100) exhibited features similar to those in Fig. 4(d).[26] The images in Figs. 4(e) and 4(f) are from simulations [for comparison with the data in Fig. 4(d)] and are discussed in Sec. IVC.

The diffraction images were binned horizontally (vertically) and the background intensity was subtracted to obtain cross sections along Q_z (Q_x). Representative binned vertical and horizontal cross sections for Expt. 5 are shown in Figs. 5(a) and 5(b), respectively. The average longitudinal lattice compressions ($\Delta d/d_0$, where d is the interplaner spacing of the probed *hkl* planes) were obtained from the shifts in Q_x and are shown in Fig. 6 as a function of the density compression ($\rho/\rho_0 - 1$). The results shown in Fig. 6 are in excellent agreement with past work on LiF;[3–6] as such, the average lattice compression results are not discussed here. The microstructure determination, the focus of this work, is discussed next.

IV. ANALYSIS AND DISCUSSION

A. Microstructural model and analysis approach

In general, extracting microstructural parameters from XRD data requires a model microstructure. Although it is generally accepted that stress relaxation in LiF shock compressed along [100] occurs through the motion of dislocations,[20,21,23–25,27] the existing models for shocked LiF are continuum in nature. Hence, they do not explicitly consider dislocations, and they cannot predict the heterogeneous microstructure observed in our data. Therefore, to aid data analysis, we approximate the shocked LiF as consisting of a microstructure defined by three phenomenological parameters as described next. The shocked LiF single crystal is assumed to subdivide into cubic coherently diffracting domains (CDDs) of size ζ_{CDD}. The defect type(s) responsible for the CDD size is not explicit in our model, but can, in principle, include dislocations. Each CDD is assumed to have small random rotations about the y- and z-axes relative to the ambient crystal orientation. Additionally, each CDD has a small uniform random lattice strain along the loading direction relative to the average longitudinal strain. The random rotations and longitudinal microstrains are assumed to follow Gaussian distributions with FWHMs of $\Delta\Phi_y = \Delta\Phi_z$ and $\delta d/d$, respectively. Data analysis and simulations using this framework are presented next.

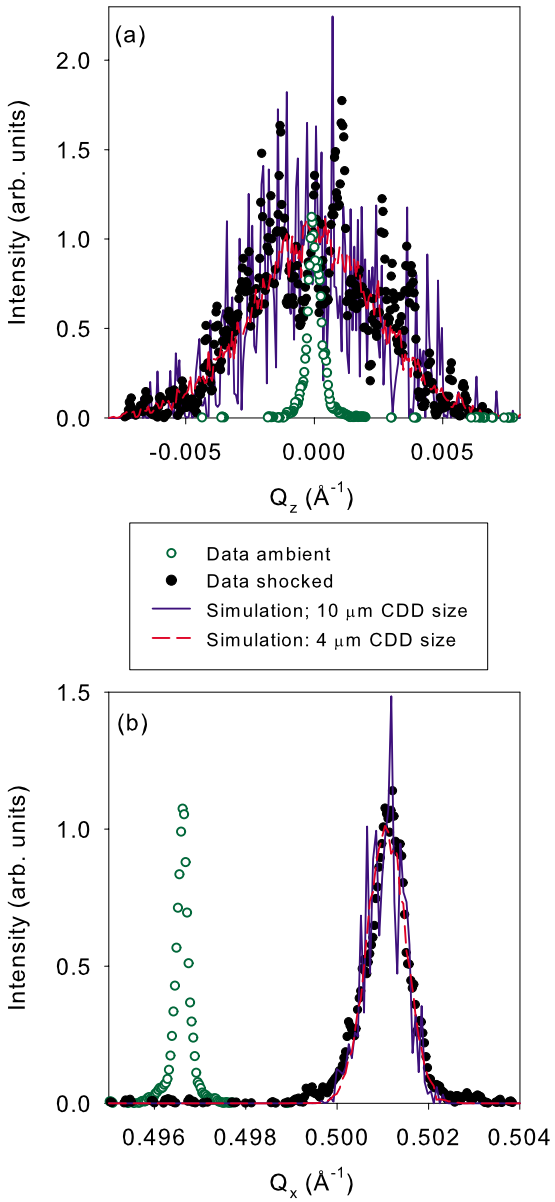

FIG. 5. (Color online) Binned cross sections of the measured [Figs. 4(c) and 4(d)] and simulated [Figs. 4(e) and 4(f)] diffraction patterns for Expt. 5. (a) shows binned vertical cross sections and (b) shows binned horizontal cross sections.

B. Analysis of diffraction pattern broadening

For the geometry used, shock-induced changes to the lattice affect the distribution of scattered intensity in reciprocal space as follows. A compression of the lattice along the loading direction causes the diffracted intensity to shift from $Q_{x,0}$ to a higher Q_x. A distribution of microstrains along the shock loading direction causes the diffracted intensity to smear over a range of Q_x values. Symmetric distributions of small angle microlattice-plane rotations around the z- and y-axes cause the diffracted intensity to smear over a range of Q_y and Q_z values centered about $Q_y = Q_z = 0$, respectively. For the geometry used, the diffracted image on the area detector is related primarily to the diffraction vector components Q_x (horizontally) and Q_z (vertically) and is insensitive to Q_y. Hence, in the absence of broadening due to small CDDs, the vertical growth of the diffraction pattern is due to a distribu-

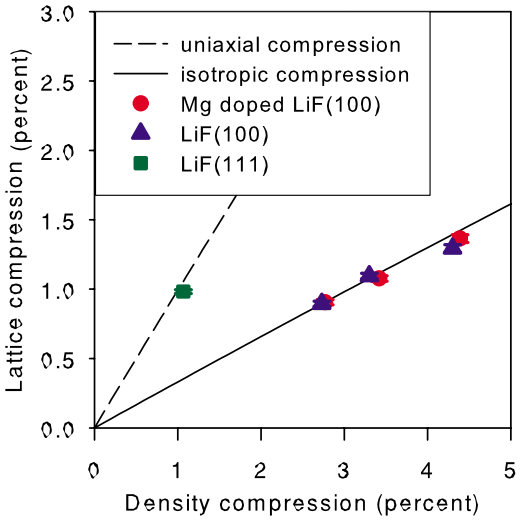

FIG. 6. (Color online) Measured lattice compression (on average) along the shock propagation direction and the corresponding calculated density compression are plotted. As described in Ref. 3, the dashed and solid lines are the expected relationships between the lattice and density compressions for uniaxial (slope=1) and isotropic (slope≈1/3) lattice compressions, respectively.

tion of microlattice-plane rotations (about the y-axis) and the horizontal growth of the diffraction pattern is due to a distribution of longitudinal microstrains. If the CDD size ζ_{CDD} of the shocked crystal is small enough, an additional broadening of the diffraction pattern will occur.

1. Microlattice-plane rotations

For nonzero Φ_y, the reciprocal lattice vector under investigation $\vec{Q}$ develops a z-component Q_z. For small Φ_y, $\Phi_y \approx Q_z/|\vec{Q}|$, where $|\vec{Q}|=2 \sin\theta/\lambda$. Hence, an increase in the measured cross section width along Q_z means that the shocked crystal has a distribution of microlattice-plane rotations Φ_y about the y-axis. Figure 5(a) shows that significant shock-induced broadening of the cross section along Q_z occurred for LiF(100). Fitting the measured cross sections along Q_z to Gaussians matched the data within experimental resolution. The FWHM, ΔQ_z, is related to the FWHM of the angular distribution of microlattice-plane rotations about the y-axis ($\Delta\Phi_y$) through $\Delta\Phi_y=[\lambda\Delta Q_z/(2 \sin\theta)180°/\pi]$. The distribution of Φ_y values is near continuous and peaks at the orientation of the ambient crystal, $\Phi_y=0$. Although our measurement is insensitive to the distribution of microlattice-plane rotations about the z-axis, it should be the same as the measured distribution about the y-axis because of the fourfold rotational symmetry about the LiF [100] axis.

Values for $\Delta\Phi_y$, after subtracting the vertical instrumental broadening, are shown in Fig. 7(a). Microlattice-plane rotations were not observed for elastic deformation in shocked LiF(111). In contrast, microlattice-plane rotational spreads were found to increase roughly linearly with impact stress in shocked LiF(100) and reached a value of about 1.2° for the Mg-doped LiF sample shocked to the highest stress (Expt. 7).

We note that the effect of small CDD size was not considered when determining values for $\Delta\Phi_y$ from the vertical

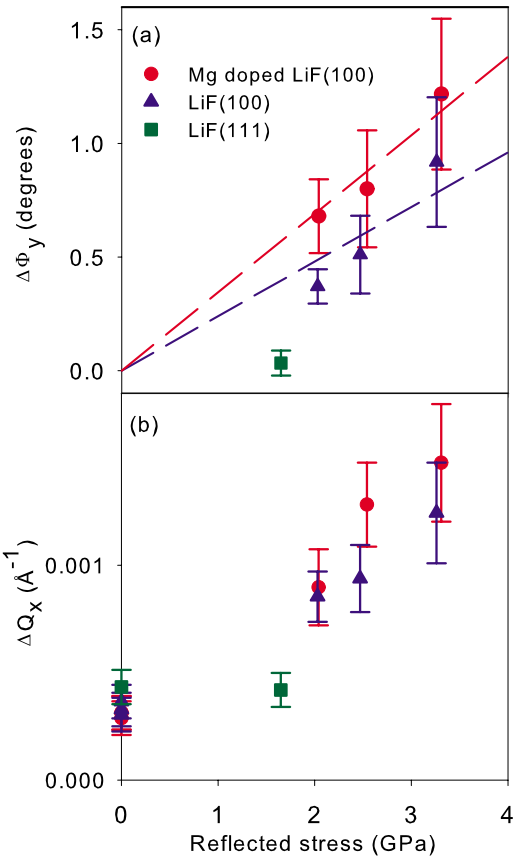

FIG. 7. (Color online) (a) Shock-induced (100) microlattice-plane rotational spread (FWHM), $\Delta\Phi_y$, in LiF. The dashed lines represent linear fits to the data constrained to pass through the origin. (b) FWHM of diffraction peak, ΔQ_x, in reciprocal space. The peak widths under ambient conditions are shown at zero stress and are caused primarily by instrumental broadening. Elastic compression along [111] is shown as a reference.

broadening of the diffraction peaks. This was not necessary because the effect of small CDD size is to broaden the diffraction pattern approximately equally in Q_x and Q_z; the measured growth in Q_x, which provides an upper bound for broadening due to CDD size, is significantly smaller than the measured growth in Q_z.

2. Microstrains and CDD size

An increase in the measured cross section width along Q_x means that the shocked crystal developed a distribution of microlattice-strains along the loading direction and/or the size of the CDDs was reduced relative to the ambient crystal. The measured cross sections along Q_x were fit to Gaussians, and the FWHM (ΔQ_x) values are shown in Fig. 7(b) both prior to and following shock compression. ΔQ_x did not increase for the elastic deformation in shocked LiF(111) but increased substantially for the elastic-plastic deformation in shocked LiF(100). Although the present data are not sufficient to fully separate the effects of microstrains and CDD size on the shock-induced increase in ΔQ_x, we can place bounds on the two parameters. For example, the value of ΔQ_x obtained from the highest stress experiment (Expt. 7) on Mg-doped LiF(100) allows us to place an upper bound of ~0.3% FWHM on the microlattice-strain distribution. For

the same experiment, we obtain a lower bound of ~0.1 μm for the size of CDDs from the Scherrer equation.[28]

3. Loading history dependence

Although it is well established that Mg-doped LiF(100) and ultrapure LiF(100) shocked to the same peak stress undergo very different loading paths,[21] previous XRD studies on shocked LiF were not able to resolve any differences between the lattice responses of ultrapure and Mg-doped LiF(100).[3–6] The present results demonstrate that the shocked Mg-doped LiF(100) is more disordered than the shocked ultrapure LiF(100); both $\Delta\Phi_y$ and ΔQ_x were larger for the Mg-doped LiF(100) than for the ultrapure LiF(100) shocked to the same peak stress. This finding demonstrates that the microstructural changes in the peak state depend on the loading path to the peak state. The shocked Mg-doped LiF(100) samples developed more substructure than the shocked ultrapure LiF(100) samples because the Mg-doped LiF(100) samples sustained larger stress deviators resulting in larger plastic strain rates (and stress relaxation) than the ultrapure LiF samples.[21]

4. Diffraction simulations

Simulated diffraction patterns to be compared with the data in Fig. 4(d) are shown in Figs. 4(e) and 4(f). The diffraction simulations were performed by discretizing the volume of LiF exposed to the incident beam into cubic CDDs of volume ζ_{CDD}^3 and using the kinematical approximation to calculate the diffraction from each CDD. The Gaussian approximation for the intensity scattered from a small crystallite was used.[28] The following microstructural parameters were used: $\Delta\Phi_y=\Delta\Phi_z=0.68°$, $\delta d/d=0.2\%$, and $\zeta_{\mathrm{CDD}}=4$ μm [Fig. 4(e)] and 10 μm [Fig. 4(f)]. Hence, the simulations include diffraction pattern shape changes due to microlattice-plane rotations, microstrains, and broadening due to small crystallite size. The location of the simulated diffraction pattern centers were determined by setting the average value of Q_z to zero (as was done for the experimental data) and the average value of Q_x to the average value measured in the experiment; the purpose of the simulations is only to compare the broadening. Binned vertical and horizontal cross sections of the images in Figs. 4(e) and 4(f) are shown in Figs. 5(a) and 5(b), respectively. Overall, the vertical and the horizontal cross sections of the data match the horizontal and the vertical cross sections of the simulations within experimental resolution.

The graininess apparent in the simulations is the result of the finite number of CDDs satisfying the diffraction condition. Only a small fraction of the CDDs are oriented properly with respect to the local incident wavevector to contribute non-negligibly to the diffraction pattern. Increasing ζ_{CDD} increases the graininess of the simulation and for $\zeta_{\mathrm{CDD}}=10$ μm [Fig. 4(f)], the graininess is similar to that observed in the experiment. Hence, the simulation results allow us to place an upper bound of ~10 μm on the size of CDDs in the shocked LiF. It is important to note that this is an upper bound; the actual CDD size may be smaller because the graininess in the experimental data is in large part due to photon statistics and the data would likely be smoother with a larger number of incident photons. Future measurements with a larger number of incident photons and a smaller volume of crystal exposed to the beam should be useful in determining more precisely the size of the CDDs.

V. CONCLUDING REMARKS

The present work has demonstrated that a third generation synchrotron can be used successfully to obtain real-time XRD data from a shocked crystal in plate impact experiments. The ability to obtain such data while the sample is in a state of macroscopic uniaxial strain represents a significant development to probe microscopically shock-induced deformation and structural changes.

Using the experimental developments indicated here, elastic and elastic-plastic deformations were examined in shocked LiF single crystals. As expected,[3–6] the average lattice compression was uniaxial for elastic deformation and isotropic for elastic-plastic deformation. The focus of the present work was on the XRD broadening data. The broadening results showed that LiF crystals shocked along [100] develop a substructure which consists of CDDs with size of 0.1–10 μm and a distribution of (100) microlattice-plane rotations of order 1° wide. In contrast, no broadening was observed for elastic deformation due to shock compression along the [111] orientation.

The experimental approach described is sensitive enough to detect microstructural differences due to loading history variations between shock compressed pure LiF and Mg-doped LiF samples. We are able to simulate the measured diffraction patterns by considering diffraction from a model LiF(100) sample with a heterogeneous substructure defined by a size for CDDs, a Gaussian distribution of longitudinal microstrains, and Gaussian distributions for microlattice-plane rotations. Improvements in the analysis and simulations can be made as data become available. In particular, future work utilizing diffraction peak broadening of multiple *hkl* reciprocal lattice points will better separate the effects of microstrains and CDD size on the diffraction pattern broadening. Such measurements will also provide further physical insight into the micromechanisms occurring during shock-induced elastic-plastic deformation by exploring microstructural anisotropy.

In closing, we point out that the present work represents a start. Neither the synchrotron beamlines and optics nor the detection capabilities were optimal in these initial experiments. Significant improvements in the incident x-ray flux and detectors can be made to interface synchrotron capabilities with shock compression experiments in an optimal manner.

ACKNOWLEDGMENTS

Nate Arganbright is thanked for assistance with sample preparation. Cory Bakeman is thanked for assistance with the plate impact experiments. Beamtime was supported by the HPCAT member institutions (CIW, CDAC, LLNL, and UNLV). Dave Mao (CIW) and Rus Hemley (CDAC) are thanked for donating some of their beamtime. Peter Lier-

mann is thanked for assistance in obtaining safety approval. Assistance with the experimental setup was provided by Eric Rod, Paul Chow, and Peter Liermann (all at HPCAT). Paul Chow, Peter Liermann, Yang Ding (HPSynC), and Wenge Yang of HPCAT are thanked for beamline assistance during the experiments. This work was supported primarily by the DOE Grant No. DE-FG03-97SF21388.

Portions of this work were performed at HPCAT (Sector 16), Advanced Photon Source (APS), Argonne National Laboratory. HPCAT is supported by DOE-BES, DOE-NNSA, NSF, and the W. M. Keck Foundation. APS is supported by DOE-BES under Contract No. DE-AC02-06CH11357.

[1]Y. M. Gupta, in *Encyclopedia of Physics*, edited by R. M. Besancon (Van Nostrand Reinhold, New York, 1985), pp. 1109–1115.
[2]Q. Johnson, A. Mitchell, R. N. Keeler, and L. Evans, Phys. Rev. Lett. **25**, 1099 (1970); Q. Johnson, A. C. Mitchell, and L. Evans, Appl. Phys. Lett. **21**, 29 (1972).
[3]P. A. Rigg and Y. M. Gupta, Appl. Phys. Lett. **73**, 1655 (1998).
[4]P. A. Rigg and Y. M. Gupta, Phys. Rev. B **63**, 094112 (2001).
[5]B. J. Jensen and Y. M. Gupta, J. Appl. Phys. **100**, 053512 (2006).
[6]Y. M. Gupta, K. A. Zimmerman, P. A. Rigg, E. B. Zaretsky, D. M. Savage, and P. M. Bellamy, Rev. Sci. Instrum. **70**, 4008 (1999).
[7]E. Zaretsky, J. Appl. Phys. **93**, 2496 (2003).
[8]A. Loveridge-Smith, A. Allen, J. Belak, T. Boehly, A. Hauer, B. Holian, D. Kalantar, G. Kyrala, R. W. Lee, P. Lomdahl, M. A. Meyers, D. Paisley, S. Pollaine, B. Remington, D. C. Swift, S. Weber, and J. S. Wark, Phys. Rev. Lett. **86**, 2349 (2001).
[9]C. S. Smith, Trans. AIME **212**, 574 (1958).
[10]E. Hornbogen, Acta Metall. **10**, 978 (1962).
[11]M. A. Meyers, Scr. Metall. **12**, 21 (1978).
[12]E. Zaretsky, J. Appl. Phys. **78**, 3740 (1995).
[13]M. A. Meyers, F. Gregori, B. K. Kad, M. S. Schneider, D. H. Kalantar, B. A. Remington, G. Ravichandran, T. Boehly, and J. S. Wark, Acta Mater. **51**, 1211 (2003).
[14]B. L. Holian and P. S. Lomdahl, Science **280**, 2085 (1998).
[15]E. M. Bringa, K. Roslankova, R. E. Rudd, B. A. Remington, J. S. Wark, M. Duchaineau, D. H. Kalantar, J. Hawreliak, and J. Belak, Nature Mater. **5**, 805 (2006).
[16]P. Kumar and R. J. Clifton, J. Appl. Phys. **50**, 4747 (1979).
[17]J. E. Vorthman and G. E. Duvall, J. Appl. Phys. **53**, 3607 (1982).
[18]A. L. Stevens and O. E. Jones, ASME J. Appl. Mech. **30**, 359 (1972).
[19]The experimental details will be provided in a future publication.
[20]J. R. Asay, G. R. Fowles, G. E. Duvall, M. H. Miles, and R. F. Tinder, J. Appl. Phys. **43**, 2132 (1972).
[21]Y. M. Gupta, G. E. Duvall, and G. R. Fowles, J. Appl. Phys. **46**, 532 (1975).
[22]Y. M. Gupta, Appl. Phys. Lett. **26**, 38 (1975).
[23]Y. M. Gupta, J. Appl. Phys. **48**, 5067 (1977).
[24]J. R. Asay, D. L. Hicks, and D. B. Holdridge, J. Appl. Phys. **46**, 4316 (1975).
[25]J. M. Winey and Y. M. Gupta, J. Appl. Phys. **99**, 023510 (2006).
[26]For Expt. 2, two distinct images were observed in the shocked state. One was centered at $Q_z=0$ and the other was centered at higher Q_z. The two images are of similar size and our analysis only considers the image centered at $Q_z=0$.
[27]For a review of past LiF shock work see J. N. Johnson, in *High-Pressure Shock Compression of Solids*, edited by J. R. Asay and M. Shahinpoor (Springer-Verlag, New York, 1993), p. 226.
[28]B. E. Warren, *X-ray Diffraction* (Dover, New York, 1990).